Lee and Mok *Pacific Journal of Mathematics for Industry* (2016) 8:4
DOI 10.1186/s40736-016-0023-y

Pacific Journal of Mathematics for Industry
a SpringerOpen Journal

ORIGINAL ARTICLE Open Access

# Cylindrical electromagnetic waves with radiation and absorption of energy

Hyoung-In Lee[1,3*] and Jinsik Mok[2]

**Abstract**

Cylindrical electromagnetic waves have been examined mostly with a radiation condition applied at the radial far field. In modern optical technology, there are however growing number of applications where both radiation and absorption of energy should be taken into account. In order to illustrate the ramifications of such energy balance, we take plasmonic waves propagating around a metallic nanowire as an example. Hence, we provide both key mathematical formulas and corresponding numerical results for the collective electronic motions in resonance with electromagnetic waves. Firstly, we show theoretically why a net Poynting energy flow is directed inward to the cylindrical axis. Secondly, we invoke a Cauchy-Schwarz inequality for complex variables in deriving an upper bound on the specific transverse light spin along the axial direction. Thirdly, we could identify both first- and second-order polarizations. Overall, loss-induced and gain-compensated characteristics are illustrated for a dissipative system. In addition, the stability of neutral states are examined by relaxing the angular periodicity.

**Keywords:** Radiation, Absorption, Plasmonics, Neutrality, Polarization, Light spin, Upper bounds, Angular mode number

## 1. Introduction

Cylindrical electromagnetic waves around a cylindrical obstacle have been investigated for a long time [15]. For instance, optical fibers and nano-scale probes rely on wave propagations along the cylindrical axis [8, 9, 18]. Even when waves are allowed to propagate only on a plane including the cross-sectional plane of a wire, there are numerous technological applications.

For instance, consider whispering-gallery modes (WGMs) involving cylindrical waves. WGMs are employed not only for chemical and biological sensors [8, 13, 41], but also for quantum information processing [34]. Field focusing via WGMs is essential in realizing photon manipulations [28]. Numerous examples are also found in manipulating nano-objects immersed in electromagnetic fields [8, 25]. In microfluidics, rotational waves are utilized for determining fluid viscosity as well [36]. As regards applications to electronics industry, integrated photonic circuits are under a hot pursuit as a candidate replacing conventional integrated electronic circuits for reasons of low energy consumption [10]. Our recent work on graphene-coated nanowires offers additional application areas [17].

Most of these applications have been successfully analyzed as regards the energy transfer from the cylindrical objects into the surrounding environments via the century-old radiation condition [33, 41]. In addition to the mathematical aspects of the radiation condition, a variety of application areas are mentioned in [16, 33] such as radars and wireless communications.

According to this radiation condition, only outgoing waves are allowed from a body immersed in a free space in the context of exterior boundary value problems [33], thereby ensuring the well-posedness of mathematical problems [11]. This radiation condition has been built even into modern commercial numerical codes for solving Maxwell's equations [10, 16].

In fluid dynamics, it is true in the absence of energy sources in the far field of the exterior region [23]. However, in modern optical applications, there are a few exceptions, where incoming energy from afar should be taken into consideration. As an example, optical trapping of ions rely on energy supply from outside through laser illumination [27]. As another example, optical gain media for metamaterials act as energy

* Correspondence: hileesam@naver.com
[1]Research Institute of Mathematics, Seoul National University, Gwanak-gu, Seoul 08826, South Korea
[3]Computational Sciences, Korea Institute for Advanced Study, Dongdaemun-gu, Seoul 02455, South Korea
Full list of author information is available at the end of the article

sources, thus compensating energy dissipation by metallic constituents [3, 10, 39].

Figure 1(a) shows a cross-section of a cylindrical nanowire along with the cylindrical coordinates $(r, \theta, z)$ and Cartesian coordinates $(x, y, z)$. The wire radius is fixed to be $R$. We emphasize that only planar waves propagating on a plane including the cross-sectional plane of a nanowire are under current investigation. In other words, there are no wave propagations along the axial $z$-direction. Hence, we are dealing with two-dimensional wave problems, where all the field variables depend only on $(r, \theta)$ or $(x, y)$ [4, 11, 16, 33]. Our wave configuration is thus suitable for realizing topological photonics [32], if some material asymmetries are additionally provided.

In comparison, Fig. 1(b) shows a pair of two-dimensional structures, which require however three-dimensional descriptions. This configuration is hence not under direct consideration in this study. Notice in Fig. 1(a) that the metal part is convex toward the surrounding medium [4]. This radiative attenuation of waves is quite natural with such configurations. The opposite case of concave metal parts is discussed in [4], where local energy absorption takes place more easily.

Classical electromagnetic waves are governed by Maxwell's equations. They are linear partial differential equations (PDEs) for both electric and magnetic field variables in the absence of explicit current sources [15]. Suppose that all the field variables are assumed to follow the common phase factor $\exp(im\theta)$ [41]. Here, $m$ is the angular mode index, which is integer if angular periodicity prevails, i.e., $m \in \mathbb{Z}$. The PDEs are then separable into ordinary differential equations (ODEs) thanks to $m$ [40].

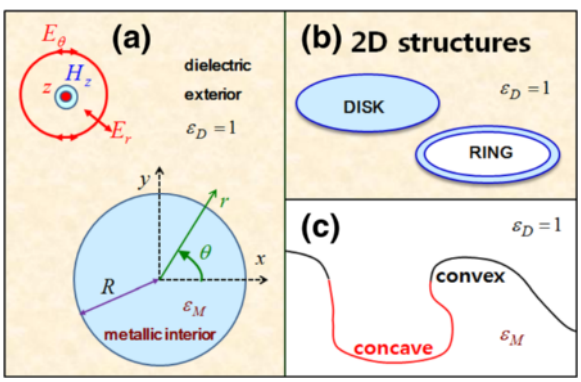


**Fig. 1 a** Schematics of primary concern to this study for a transverse magnetic (TM) wave along with both coordinates and non-zero field variables [8, 11]. **b** Three-dimensional waves around a two-dimensional disk or a ring not under current investigation [10]. **c** A generic curved or bent interface between metal and vacuum. Indicated are typical convex and concave portions towards the vacuum [4]

Consider furthermore a two-wave-interaction function $G^D_{m,A}(u)$ for a real parameter $u > 0$.

$$G^D_{m,A}(u) \equiv (1-A)H^{(1)}_m(u) + (1+A)H^{(2)}_m(u). \tag{1.1}$$

Here, $H^{(1)}_m(u)$ and $H^{(2)}_m(u)$ are Hankel functions of first and second kinds. Therefore, $H^{(1)}_m(u)$ and $H^{(2)}_m(u)$ imply waves respectively outgoing and incoming in the radial direction [2, 11, 33].

In addition, $A$ is the asymmetry parameter with $A \equiv A_r + iA_i$ so that $A \in \mathbb{C}$ and $A_r, A_i \in \mathbb{R}$. When $A \neq 0$, $A$ denote the deviation from a perfect balance between outgoing and incoming waves [31]. Notice that the ideal situation with the combined conditions $u \in \mathbb{R}$ for loss-free metals and $A = 0$ implies standing waves since $H^{(1)}_m(u) + H^{(2)}_m(u) = 2J_m(u)$ in this case [31, 33].

As an exterior boundary condition, the wave portion represented by $H^{(2)}_m(u)$ in Eq. (1.1) accounts for energy sources, without directly incorporating any source terms in the governing PDEs. Assuming the exterior outside the cylinder to be energy-conserving, non-zero values of $A$ correspond to the interior inside the cylinder being energy-dissipating. Figure 1(a) indicates that the interior is filled with metals. Therefore, the collective electronic motions in metals are in resonance with electromagnetic waves [10, 28], which are called plasmonic waves [29].

Through this example of plasmonic waves, we are here to explain several consequences resulting from the energy balance between the radiating outgoing waves and the absorptive incoming waves. By way of both mathematical analysis and numerical computations, we will find neutral states by such balanced energy exchanges. In addition, we will show how delicately those neutral states are established [4, 14, 26].

Furthermore, we will present several characteristics of cylindrical electromagnetic plasmonic waves. Firstly, Poynting energy flows will be analyzed and key analytic formulas will be derived [4]. Besides, associated implications to scattering will be discussed [9, 16, 28, 37, 41].

Secondly, we will show the existence of transverse light spins even in the absence of axial waves [6, 7]. The light spin receives an increasing attention these days because of both direct and inverse Faraday effects [17, 30, 32]. However, the intensive discussions on light spins provided in [7] center around rectilinear waves. In contrast, we are dealing here with light spins for cylindrical waves. In these respects, several interesting findings of this study are based on the following Cauchy-Schwarz inequality for $E_r, E_\theta \in \mathbb{C}$.

$$\mathrm{Im}\left(E^*_r E_\theta\right) \leq |E_r||E_\theta|. \tag{1.2}$$

Here, $(E_r, E_\theta)$ indicate the two cross-sectional components of electric field. Via this inequality, a specific spin

defined as the reduced light spin per energy density turns out to be bounded in its magnitude. This specific spin is similar to the conventional degree of electric-field polarization, but they are not equal [24, 38]. Besides, the discontinuity of specific spin across the cylindrical interface is thus illustrated. Along with optical chirality [35], light spin characterizes asymmetric structural properties of molecules or small particles on which light is illuminated.

Thirdly, the phase singularity found at the cylindrical axis is related to optical vortices [5]. The electric-field polarization will be discussed from a viewpoint of light spin and the two-dimensionality of electromagnetic waves [1, 31, 40]. Several analogies are made to fluid dynamics concerning singularity and vortices as needs arise [19].

This study complements our previous published works, since several key mathematical proofs are made here for the mostly numerical results presented by our earlier publications on electromagnetic waves in general [20] and cylindrical waves in particular [21, 22]. We remark once more that all of our previous works have accounted only for radiating waves but not the absorbing waves. In terms of the types of PDEs, the metallic loss leads to hybrid nature of hyperbolic and parabolic PDEs [11, 20, 40, 41] which render highly non-trivial all the involved numerical computations.

## 2. Problem formulation

Consider Maxwell's equations in the absence of electric charges and for nonmagnetic media [4, 15].

$$\begin{cases} \textit{Coulomb}: & \nabla\cdot\vec{\mathcal{E}}=0 \\ \textit{Ampère}: & \nabla\times\vec{H}=\varepsilon\tilde{\varepsilon}_0\dfrac{\partial\vec{\mathcal{E}}}{\partial t} \\ \textit{Faraday}: & \nabla\times\vec{\mathcal{E}}+\tilde{\mu}_0\dfrac{\partial\vec{H}}{\partial t}=0 \\ \textit{Gauss}: & \nabla\cdot\vec{H}=0 \end{cases}. \tag{2.1}$$

Both electric field vector $\vec{\mathcal{E}}$ and magnetic field vector $\vec{H}$ are real. The properties of vacuum are the electric permittivity $\tilde{\varepsilon}_0>0$ and magnetic permeability $\tilde{\mu}_0>0$. An electromagnetic medium is characterized by its relative permittivity $\varepsilon$ with $\varepsilon\in\mathbb{C}$. For instance, $\varepsilon=1$ for vacuum. For metals in a cylindrical nanowire, the interaction between electrons in metals and electromagnetic waves is incorporated into $\varepsilon(\omega)$ as a function of frequency $\omega$ according to linear response theory [15]. We assume $\omega>0$ throughout this study.

If all the field variables are assumed to follow the combined phase factor $\exp(im\theta-i\omega t)$, the normalized electric field vector $\vec{E}$ and magnetic field vector $\vec{H}$ are defined as follows [7].

$$\begin{cases} \vec{\mathcal{E}} \equiv \dfrac{1}{\sqrt{\tilde{\varepsilon}_0}}\mathrm{Re}\left[\vec{E}\ \exp(im\theta-i\omega t)\right] \\ \vec{H} \equiv \dfrac{1}{\sqrt{\tilde{\mu}_0}}\mathrm{Re}\left[\vec{H}\ \exp(im\theta-i\omega t)\right] \end{cases}. \tag{2.2}$$

In terms of $\vec{E}$ and $\vec{H}$, the Ampère law and Faraday's law in Eq. (2.1) now read $\nabla\times\vec{H}=-ik_0\varepsilon\vec{E}$ and $\nabla\times\vec{E}=-ik_0\varepsilon\vec{H}$, respectively. Here, the vacuum wave number $k_0$ is defined by $k_0\equiv\omega/c_0$, where $c_0$ is the light speed in vacuum defined by $c_0\equiv1/\sqrt{\tilde{\varepsilon}_0\tilde{\mu}_0}$.

The upper left portion of Fig. 1(a) shows a transverse-magnetic (TM) wave with its non-zero field components $(E_r, E_\theta, H_z)$ [10]. The interior in the range $0\le r<R$ refers to the metallic nanowire. In comparison, the exterior in the range $R<r$ refers to the surrounding dielectric, which is taken to be vacuum in this study. Hence, the cylindrical metal-dielectric (M-D) interface is located at $r=R$. Whenever necessary, replacements should be made such that $H_z\to H_z^{M,D}$ and $\varepsilon\to\varepsilon_{D,M}$ respectively for the interior and exterior. In this notation, $\varepsilon_D=1$.

As a data, the light wavelength is fixed at $\lambda=600\,nm$ with $\lambda\equiv2\pi c_0/\omega$, while the nanowire radius is taken to be $R=600\,nm$ on the nanometer scales. In addition, $m/R$ is called the surface wave number [4]. The relative dielectric constant $\varepsilon_M(\omega)$ of metal is $\varepsilon_M=-8.93+0.979i$ as read from [12] for gold at $\lambda=600\,nm$, thus lying in the range of visible light. Notice that $\mathrm{Im}(\varepsilon_M)=0.979$ stands for metallic loss, which leads to the dissipative attenuation of plasmonic waves [4].

Maxwell's equations give rise to the following two auxiliary relations [4].

$$E_r=-\frac{m}{\varepsilon k_0 r}H_z,\quad E_\theta=-i\frac{1}{k_0\varepsilon}\frac{dH_z}{dr}. \tag{2.3}$$

When Eq. (2.3) is plugged into Eq. (2.1), $H_z$ is found to be governed by the following Helmholtz equation [11, 28, 33, 36].

$$\frac{1}{r}\frac{d}{dr}\left(r\frac{dH_z}{dr}\right)+\left(\varepsilon k_0^2-\frac{m^2}{r^2}\right)H_z=0. \tag{2.4}$$

The reduced radial coordinate $\rho\equiv r/R$ is defined so that $0\le\rho\le1$ in the interior and $1\le\rho<\infty$ in the exterior.

Hence, $\rho = 1$ refers to the cylindrical M-D interface. In addition, the size parameter $q$ is defined below.

$$q \equiv \frac{2\pi R}{\lambda} \equiv \frac{\omega R}{c_0} \equiv k_0 R > 0. \tag{2.5}$$

From our data of $R = 600\,nm$ and $\lambda = 600\,nm$, $q = 2\pi$. Let us summarize our data for future reference [4, 10, 12, 16, 28].

$$\left.\begin{array}{l} R = 600nm \\ \lambda = 600nm \end{array}\right\} \Rightarrow \quad q = 2\pi$$
$$\left\{\begin{array}{l} \varepsilon_M = -8.93 + 0.979i \\ \varepsilon_D = 1 \end{array}\right. . \tag{2.6}$$

Since Maxwell's equations are linear, the magnetic field can assume the following normalized forms respectively in the interior and exterior [17, 18, 36].

$$\left\{\begin{array}{ll} H_z^M(\rho) = \dfrac{I_m\left(\sqrt{-\varepsilon_M}q\rho\right)}{I_m\left(\sqrt{-\varepsilon_M}q\right)} = \dfrac{J_m\left(\sqrt{\varepsilon_M}q\rho\right)}{J_m\left(\sqrt{\varepsilon_M}q\right)}, & \rho < 1 \\ H_z^D(\rho) = \dfrac{G_{m,A}^D(q\rho)}{G_{m,A}^D(q)}, & \rho > 1 \end{array}\right. . \tag{2.7}$$

Here, $G_{m,A}^D(u)$ is as defined in Eq. (1.1). Besides, $I_m(\beta) = i^{-m} J_m(i\beta)$ for complex $\beta$ renders identical the two expressions for $H_z^M(\rho)$ in Eq. (2.7). Hence, Eq. (2.7) represents spatially inhomogeneous fields necessary to detect asymmetric optical properties of matters immersed in our light fields [35].

A subtle requirement $-\pi < \arg(\beta) \le \frac{1}{2}\pi$ is satisfied by ensuring $\sqrt{\varepsilon_M} = 0.163 + 2.99i$, but not $\sqrt{\varepsilon_M} = 0.163 - 2.99i$ [2]. This fact is in conformity to the causality condition accompanied by the phase factor $\exp(-i\omega t)$ with $\omega$, $t \ge 0$. It is numerically confirmed for $i\beta \propto \sqrt{\varepsilon_M}$ that $\arg(\beta) = \arg(2.99 - i0.163) = -0.0546$. By the way, the choice $\mathrm{Im}(\varepsilon_M) > 0$ is in line with the selection of the outgoing waves in the absence of energy sources [4, 16, 23, 33].

Let us define the logarithmic derivative $\partial_{\log}[F(\beta)]$ [4, 5].

$$\begin{aligned} \partial_{\log}[F(\beta)] &\equiv \left\{\frac{d}{d\alpha}\ln[F(\alpha)]\right\}\Big|_{\alpha=\beta} \\ &= \left\{\frac{1}{F(\alpha)}\frac{dF(\alpha)}{d\alpha}\right\}\Big|_{\alpha=\beta} \end{aligned} . \tag{2.8}$$

Notice that this kind of logarithmic derivative is characteristic of Green functions encountered when dealing with Laplace operator in two-dimensional planar geometry [11, 16, 40].

As one of interface conditions across $\rho = 1$, the first continuity in $H_z$ leads to $H_z^M(1) = H_z^D(1)$, which has already been incorporated into Eq. (2.7). The other continuity in $\varepsilon E_r$ becomes $\varepsilon_M E_r^M(1) = \varepsilon_D E_r^D(1)$, which is identical to $H_z^M(1) = H_z^D(1)$ because of Eq. (2.3). The third continuity in $E_\theta$ is enforced such that $E_\theta^M(1) = E_\theta^D(1)$, which is translated via Eq. (2.3) into the following [4].

$$\frac{1}{\varepsilon_M}\frac{dH_z^M(\rho)}{d\rho}\bigg|_{\rho=1} = \frac{1}{\varepsilon_D}\frac{dH_z^D(\rho)}{d\rho}\bigg|_{\rho=1}. \tag{2.9}$$

Consequently, the well-known dispersion relation $\mathcal{R}_M = \mathcal{R}_D$ on resonance [4, 8–10] can be written as follows.

$$\mathcal{R}_M = \mathcal{R}_D. \tag{2.10}$$

Here, the residual function $\mathcal{R}_M$ for the interior defined as follows [4].

$$\mathcal{R}_M \equiv -\frac{\partial_{\log}\left[I_m\left(\sqrt{-\varepsilon_M}q\right)\right]}{\sqrt{-\varepsilon_M}} = \frac{\partial_{\log}\left[J_m\left(\sqrt{\varepsilon_M}q\right)\right]}{\sqrt{\varepsilon_M}}. \tag{2.11}$$

On the other hand, the residual function $\mathcal{R}_D$ for the exterior is defined as follows with the help of $G_{m,A}^D(q)$ defined previously in Eq. (1.1).

$$\begin{aligned} \mathcal{R}_D &\equiv \partial_{\log}\left[G_{m,A}^D(q)\right] \\ &\equiv \frac{(1-A)\partial_q H_m^{(1)}(q) + (1+A)\partial_q H_m^{(2)}(q)}{(1-A)H_m^{(1)}(q) + (1+A)H_m^{(2)}(q)}. \end{aligned} \tag{2.12}$$

$$\partial_q H_m^{(1,2)}(q) \equiv \frac{dH_m^{(1,2)}(q)}{dq}. \tag{2.13}$$

Notice that both $\mathcal{R}_M$ and $\mathcal{R}_D$ arise essentially from the respective field profiles given in Eq. (2.7).

From the linearity of $G_{m,A}^D(u)$ in Eq. (1.1) with respect to $A$, the dispersion relation $\mathcal{R}_M = \mathcal{R}_D$ in Eq. (2.10) along with $\mathcal{R}_M = \partial_{\log}\left[G_{m,A}^D(q)\right]$ in Eq. (2.12) takes the following bilinear form

$$\mathcal{R}_M = \frac{\gamma_1 + \gamma_2 A}{\gamma_3 + \gamma_4 A}. \tag{2.14}$$

Here, $(\gamma_1, \gamma_2, \gamma_3, \gamma_4)$ are appropriately specified as follows.

$$\begin{array}{l} \gamma_1 \equiv \partial_q H_m^{(2)}(q) + \partial_q H_m^{(1)}(q) \\ \gamma_2 \equiv \partial_q H_m^{(2)}(q) - \partial_q H_m^{(1)}(q) \\ \gamma_3 \equiv H_m^{(2)}(q) + H_m^{(1)}(q) \\ \gamma_4 \equiv H_m^{(2)}(q) - H_m^{(1)}(q) \end{array} . \tag{2.15}$$

Therefore, $A(m)$ can be readily evaluated for a pair of the already prescribed data in Eq. (2.6). We call a state with such a computed $A$ the "neutral" state.

To the best of the author's knowledge, the particular dispersion relation $\mathcal{R}_M = \mathcal{R}_D$ in Eq. (2.10) is derived

here for the first time in the presence of both energy radiation and absorption.

## 3. Limit cases

The relations presented so far admit several limit forms useful to better grasping the dynamics under investigation. In the context of gently bent interfaces as depicted in Fig. 1(c), several relevant limit forms are discussed in details in [4]. His treatment based on local curvatures along the interfaces pointed out that the convexity or concavity toward the vacuum play a crucial role in determining whether energy radiation or absorption is more dominant. In addition, we can figure out that his deduction of slowly varying or adiabatic changes in field variables had ultimately led to the notion of Berry curvature and connection, which is related to Chern-Simons theory of topological physics [32].

Firstly, in a static limit as $\omega \to 0$, Helmholtz equation is Eq. (2.4) is reduced to the following Laplace equation.

$$\frac{1}{r}\frac{d}{dr}\left(r\frac{dH_z}{dr}\right)-\frac{m^2}{r^2}H_z=0. \tag{3.1}$$

Notice that this equation is of homogeneous order with respect to the $r$-coordinate, thus admitting the general solution $H_z(\rho) = C_+\rho^m + C_-\rho^{-m}$ for $m > 0$. Here, $C_\pm$ are constants with $C_\pm \in \mathbb{C}$. For the sake of simplicity, consider only the case $H_z^M(\rho)\to 0$ as $\rho \to 0$ but $H_z^D(\rho)\to 0$ as $\rho \to \infty$. Since only a single additional interface condition is applicable, we can choose it to be $H_z^M(1) = H_z^D(1)$ instead of $E_\theta^M(1) = E_\theta^D(1)$. Instead of Eq. (2.7), we hence obtain the solution to Eq. (3.1) as follows.

$$\begin{cases} H_z^M(\rho)=\rho^m, & \rho<1 \\ H_z^D(\rho)=\rho^{-m}, & \rho>1 \end{cases}. \tag{3.2}$$

For the particular value of $m = 0$, Eq. (3.1) admits $H_z(\rho) = C_+ + C_- \ln(\rho)$ [40].

Secondly, in the high-frequency limit as $\omega \to \infty$ [16], Eq. (2.4) leads to $\left|\varepsilon k_0^2\right| \propto \left|m^2/r^2\right|$, thus requiring proportionately highly rotational speeds as well. This limit has been thoroughly analyzed in [4] under the subject of "argument < < order, order large" [2].

Thirdly, the azimuthally independent waves with $m = 0$ are of utmost interests to engineering applications for waveguides [9, 11]. But, let us mention only that the transverse-magnetic (TM) wave in this case comes with its non-zero field components ($E_r$, $H_\theta$, $E_z$) instead of ($E_r$, $E_\theta$, $H_z$) under current investigation.

Fourthly, for $A = -1$ and $\varepsilon_M = 1$, $\mathcal{R}_M = \mathcal{R}_D$ in Eq. (2.10) is reduced to the following much-studied dispersion relation [4, 9, 14, 28] in the presence solely of energy radiation.

$$\mathcal{R}_M \equiv \frac{\partial_{\log}\left[J_m\left(\sqrt{\varepsilon_M}q\right)\right]}{\sqrt{\varepsilon_M}} = \frac{1}{H_m^{(1)}(q)}\frac{dH_m^{(1)}(q)}{dq} \equiv \mathcal{R}_D. \tag{3.3}$$

Note that Eq. (3.3) is highly nonlinear in the usual eigenvalue $q$ defined in Eq. (2.5), instead of being able to be specified as in Eq. (2.6). In this case, energy radiation is represented by $H_m^{(1)}(q)$ in the absence of energy absorption. In the presence of metallic loss as given by the dielectric constant $\varepsilon_M = -8.93 + 0.979i$ as provided in Eq. (2.6), Eq. (3.3) should lead to $q$ being complex. In turn, such a complex $q$ means a complex $\omega$ according to $q \equiv \omega R/c_0$ in Eq. (2.5).

Notice furthermore that $\varepsilon_M = -8.93 + 0.979i$ has been selected from the experimentally measured data such as from [12]. Of course, the frequency-dependent data $\varepsilon_M(\omega)$ or $\varepsilon_M(\lambda)$ is provided in [12, 32, 41] as well. However, the data $\varepsilon_M(\omega)$ has been obtained only for real $\omega$, i.e., under steady states. Normally, the data $\varepsilon_M(\omega)$ with complex $\omega$ is not available. Even the phenomenological Drude formula is $\varepsilon_M(\omega) = 1 - \omega_p^2/(\omega^2 + i\omega/\tau)$ with both $\omega_p$ and $\tau$ specified so that it is supposed to be valid only for real $\omega$ [4].

In a short summary, Eq. (3.3) poses no computational difficulty in finding $q_r + iq_i$ [4], once $\varepsilon_M(\omega)$ is available. Unfortunately, such data $\varepsilon_M(\omega)$ for complex $\omega_r + i\omega_i$ is currently unavailable. This is why traditional solutions to Eq. (3.3) have been made mostly with loss-free metal with $\mathrm{Im}(\varepsilon_M) = 0$ as in [4]. In this case, $I_m\left(\sqrt{-\varepsilon_M}q\right)$ in Eq. (2.11) can be conveniently rewritten to be $I_m\left(\sqrt{|\varepsilon_M|}q\right)$ [4]. Moreover, for the generic curved interface such as displayed in Fig. 1(c), the convex and concave portions are associated more likely with $H_m^{(1)}(q)$ and $H_m^{(2)}(q)$, respectively, whereby $m$ for $\exp(im\theta)$ is then relaxed to be complex, viz., $m \in \mathbb{C}$.

Under the assumption of $\mathrm{Im}(\varepsilon_M) = 0$, we have employed $\varepsilon_M = -8.93$ for loss-free metals in solving Eq. (3.3). There is now only a radiative attenuation of rotational waves but with neither dissipative attenuation nor energy absorption from the radial far field. Meanwhile, it is necessary that $q_i < 0$ or $\omega_i < 0$ because of $q \equiv \omega R/c_0$ for waves to be attenuated as time goes on as seen from the phase factor $\exp(-i\omega t) = \exp(-i\omega_r t + i\omega_i t)$.

For the specified angular mode index $m = 1$, we found $q = 0.5694 - i0.5314$ by numerical computations. This eigenvalue is computed within the computational error $|\mathcal{R}_M - \mathcal{R}_D| < 10^{-4}$ for the residual in Eq. (3.3). In addition, there are infinitely many eigenvalues of $q$ with $|q_i| > 0.5314$ so that they are more attenuating. With varying $m$, we performed more computations.

Figure 2 shows a series of thus-found complex size parameter $q \equiv q_r + iq_i$ with varying $m$. The horizontal axis is the temporal frequency $q_r$, whereas the vertical axis is the attenuation rate $-q_i$. The most notable is the fact that the minimum in $-q_i$ is achieved with $m = 1$. In comparison, the non-rotational wave with $m = 0$ is more radiative than any other rotational waves with $m > 1$ [32]. Physically speaking, a minimally rotational wave undergoes the least attenuation, thus corroborating in part the importance of light spins. Since the curve over the range $m \geq 1$ is less steep than the linear one in Fig. 2(a), the effectiveness of rotational waves, namely, $q_r/m$ increases with $m$. Furthermore, it is supposed from Fig. 2(b) that $|q_r/m| < 1$ even as $m \to \infty$ [4].

## 4. Dispersion relation and its solutions

Our numerical results are obtained as follows. Firstly, the input data of $q = 2\pi$ and $(\varepsilon_M = -8.93 + 0.979i, \varepsilon_D = 1)$ are assigned as in (2.6). Secondly, $\mathcal{R}_M$ is evaluated from (2.11) with a specified value of $m$. Thirdly, the four parameters $(\gamma_1, \gamma_2, \gamma_3, \gamma_4)$ are computed from (2.15). Fourthly, $A$ is finally computed as follows by inverting Eq. (2.14).

$$A = \frac{\gamma_3 \mathcal{R}_M - \gamma_1}{\gamma_2 - \gamma_4 \mathcal{R}_M}. \tag{4.1}$$

Figure 3 plots the asymmetry parameter $A$ on the complex $(A_r, A_i)$-plane with varying $m$ as indicated by several integers with $0 \leq m \in \mathbb{Z}$ [36]. It turns numerically out that $A_r > 0$ for all values of $m$, thus meaning a balance falling a little in favor of energy absorption. It is because some portion of incoming energy is eventually dissipated in metal, whereas the remaining portion is reflected as radiating energy. Figure 3 contains additional straight lines that connect two values of $A$ between two adjoining neutral states with $m$ and $m + 1$.

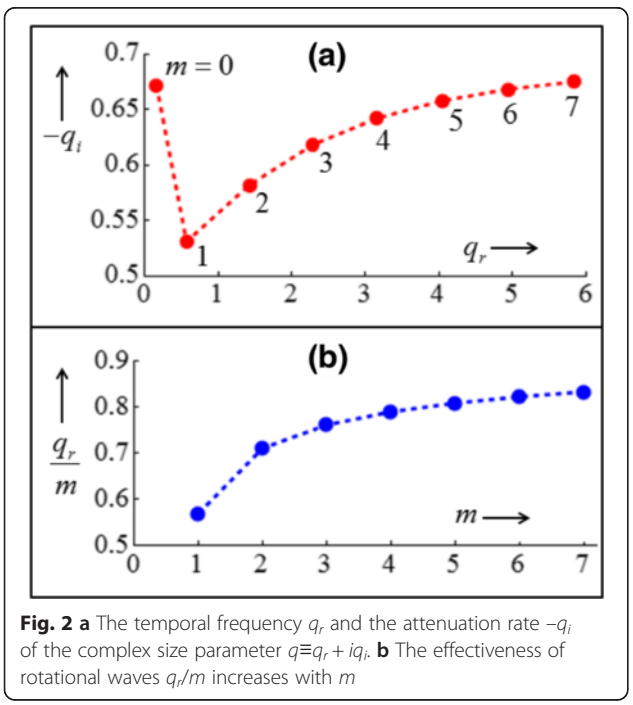


**Fig. 2 a** The temporal frequency $q_r$ and the attenuation rate $-q_i$ of the complex size parameter $q \equiv q_r + iq_i$. **b** The effectiveness of rotational waves $q_r/m$ increases with $m$

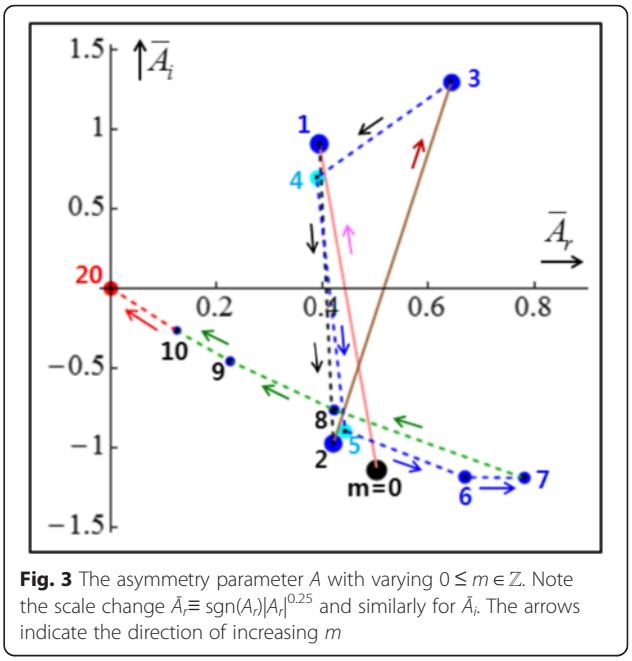


**Fig. 3** The asymmetry parameter $A$ with varying $0 \leq m \in \mathbb{Z}$. Note the scale change $\bar{A}_r \equiv \mathrm{sgn}(A_r)|A_r|^{0.25}$ and similarly for $\bar{A}_i$. The arrows indicate the direction of increasing $m$

Notice that these connecting lines do not result from computations. However, dynamics along these lines can be conjectured to be associated with non-integer values of $m$ arising from generic convex and/or concave interfaces as depicted in Fig. 1(c) [4].

Furthermore, Fig. 3 shows that the several leading neutral states over $1 \leq m \leq 7$ undergo rather erratic location changes on the complex $\bar{A}$ -plane for relatively small values of $m$. Note the scale change $\bar{A}_r \equiv \mathrm{sgn}(A_r)|A_r|^{0.25}$ and similarly for $\bar{A}_i$. In other words, $A$ moves across the real line of $A_i = 0$ with varying $m$. However, from $m = 7$ onward to $m = 20$, they follow an almost straight trajectory. Already at $m = 20$, its neutral state nearly reached its limit location at $A = 0$, viz., a perfect balance between energy radiation and absorption.

Let us review the meaning of the dispersion relation presented in Eq. (2.10), which can be understood as a complex equation $\mathcal{R}_M\left(\sqrt{\varepsilon_M} q, A\right) = \mathcal{R}_D(q, A)$. As a result, Eq. (2.10) requires the simultaneous satisfaction of the following two real relations.

$$\begin{cases} \mathrm{Re}\left[\mathcal{R}_M\left(\sqrt{\varepsilon_M} q, A\right)\right] = \mathrm{Re}[\mathcal{R}_D(q, A)] \\ \mathrm{Im}\left[\mathcal{R}_M\left(\sqrt{\varepsilon_M} q, A\right)\right] = \mathrm{Im}[\mathcal{R}_D(q, A)] \end{cases}. \tag{4.2}$$

This pair of equations are numerically solved for $A$ as an eigenvalue to the operators consisting of the domain

operator in Eq. (2.4) and the pair of boundary operators in Eq. (2.9) of Neumann type and $H_z^M(1) = H_z^D(1)$ of Dirichlet type [4, 17, 32]. Therefore, our problem can be formulated only in terms of the magnetic field $H_z^{M,D}$ along the cylindrical axis [11]. Once $A$ is found, we can view both $\mathcal{R}_M(\sqrt{\varepsilon_M}q)$ and $\mathcal{R}_D(q)$ as depending only on $q$. We then make variation in $q$, which can be alternatively achieved by introducing the aforementioned $\rho \equiv r/R$.

Recall first of all that $\varepsilon_D = 1$ along with other fixed data in Eq. (2.6). Figure 4 displays four curves: Re $\left[\mathcal{R}_M(\sqrt{\varepsilon_M}\rho q)\right]$ in red color, Re$[\mathcal{R}_D(\rho q)]$ in blue, Im $\left[\mathcal{R}_M(\sqrt{\varepsilon_M}\rho q)\right]$ in magenta, and Im$[\mathcal{R}_D(\rho q)]$ in green. As expected from the solution to the dispersion relation $\mathcal{R}_M(\sqrt{\varepsilon_M}q) = \mathcal{R}_D(q)$, the pair of broken curves for Re$\left[\mathcal{R}_M(\sqrt{\varepsilon_M}\rho q)\right]$ and Re$[\mathcal{R}_D(\rho q)]$ intersect at $\rho = 1$. Likewise, the other pair of solid curves for Im $\left[\mathcal{R}_M(\sqrt{\varepsilon_M}\rho q)\right]$ and Im$[\mathcal{R}_D(\rho q)]$ intersect at $\rho = 1$ (they do although the crossing is hardly discernible with bare eyes).

What is more important is the potential-function nature of the modified logarithmic derivatives $\mathcal{R}_M(\sqrt{\varepsilon_M}\rho q)$ and $\mathcal{R}_D(\rho q)$, as explained for Eq. (2.10). Although $\mathcal{R}_M(\sqrt{\varepsilon_M}\rho q)$ and $\mathcal{R}_D(\rho q)$ are originally defined respectively in the interior and in the exterior, both are extended in Fig. 4 respectively into the exterior and into the interior. It is thus found from Fig. 4 that both Re$\left[\mathcal{R}_M(\sqrt{\varepsilon_M}\rho q)\right]$ and Im$\left[\mathcal{R}_M(\sqrt{\varepsilon_M}\rho q)\right]$ exhibit the characteristics of infinitely attracting potential functions, thereby characterizing metals. In comparison, Re$[\mathcal{R}_D(\rho q)]$ looks like an infinitely repelling potential function. It is unique that Im$[\mathcal{R}_D(\rho q)]$ displays its minimum at a certain value of $\rho$ in the vicinity of the origin at $\rho = 0$.

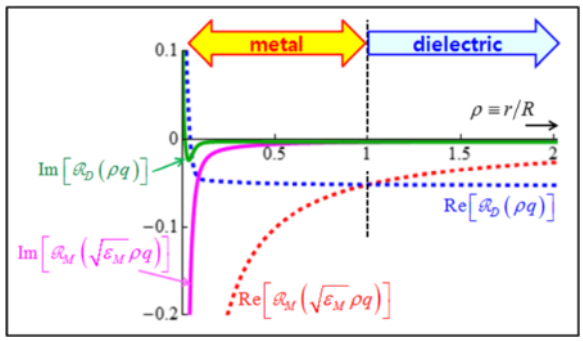


**Fig. 4** The real and imaginary parts of the modified logarithmic potentials for $m = 1$. The corresponding asymmetry parameter is $A = 0.02426 + i0.6887$

As a precaution in the following developments, we notice the following inequality as regards Eq. (2.7).

$$H_z^D(\rho q, q) = \frac{G_{m,A}^D(q\rho)}{G_{m,A}^D(q)}$$
$$\frac{dH_z^D(\rho q, q)}{d(q\rho)} = \frac{1}{G_{m,A}^D(q)}\frac{dG_{m,A}^D(q\rho)}{d(q\rho)} \quad .$$
$$\neq \frac{1}{G_{m,A}^D(q\rho)}\frac{dG_{m,A}^D(q\rho)}{d(q\rho)} \equiv \partial_{\log}\left[G_{m,A}^D(q\rho)\right] \tag{4.3}$$

Here, $H_z^D(\rho)$ is rewritten to be $H_z^D(\rho q, q)$, where $\rho q$ is a variable depending on the radial coordinate, but $q$ is a specified parameter. A similar inequality holds true to $H_z^M(\rho)$ as well.

## 5. Poynting energy flows

The energy flow of electromagnetic waves is described by Poynting vector $\vec{P} \equiv (P_r, P_\theta, P_z)$ with $\vec{P} \equiv \sqrt{|\varepsilon|}\mathrm{Re}\left(\vec{E} \times \vec{H}^*\right)$ [4, 15]. This formula is valid in a time-averaged sense for $\omega > 0$. Notice that $q \equiv k_0 R$ from Eq. (2.5), and it is specified as in Eq. (2.6). Let us evaluate each component of $\vec{P}$. Firstly, it is trivially found that $P_z^{M,D} = 0$. Secondly, $P_\theta^D = -\mathrm{Re}\left[E_r^D (H_z^D)^*\right]$, which becomes via Eq. (2.3) $P_\theta^D = m(\rho q)^{-1}\left|H_z^D\right|^2$. Hence, $P_\theta^D$ appears to be proportional to $m$. Notice here that we are interested mainly in the dielectric exterior.

Thirdly, $P_r^D = \mathrm{Re}\left[E_\theta^D (H_z^D)^*\right]$, which is evaluated for our particular cylindrical wave in the following way. In the dielectric exterior, Eq. (2.3) from Maxwell's equations are specialized to $E_r^D = -(m/k_0 r)H_z^D$ and $E_\theta^D = -i(k_0)^{-1}(dH_z^D/dr)$ since $\varepsilon_D = 1$. With a suitable change in the independent variable, $P_r^D$ leads to the following.

$$P_r^D(\alpha) = \mathrm{Re}\left[\left(-i\frac{1}{k_0}\frac{dH_z^D}{dr}\right)(H_z^D)^*\right]$$
$$= \left|H_z^D(\alpha)\right|^2 \mathrm{Im}\left\{\partial_{\log}[H_z(\alpha)]\right\} \quad .$$
$$= \left|H_z^D\right|^2(\alpha)\mathrm{Im}\left\{\partial_{\log}\left[G_{m,A}^D(\alpha)\right]\right\} \tag{5.1}$$

For simplicity, we employed a short-hand notation $\alpha \equiv q\rho$ for the arguments of the relevant functions in the dielectric exterior. Notice that $\alpha > 0$ from Eq. (2.5). The last step in Eq. (5.1) is taken by resorting to the $H_z^D$ -profile given in Eq. (2.7) [5, 21, 22].

For Eq. (5.1), let us analyze $G^D_{m,A}(\alpha)$ defined in Eq. (1.1) by recalling [2, 33]

$$H^{(1,2)}_m(\alpha) = J_m(\alpha) \pm iY_m(\alpha). \tag{5.2}$$

Hence, $G^D_{m,A}(\alpha)$ defined in Eq. (1.1) can be recast into

$$G^D_{m,A}(\alpha) = 2[J_m(\alpha) - iAY_m(\alpha)]. \tag{5.3}$$

Let us further define a temporary parameter $\Gamma(\alpha)$, which is related to the absolute value squared.

$$\begin{aligned}\Gamma(\alpha) &\equiv |J_m(\alpha)|^2 + |A|^2 |Y_m(\alpha)|^2 \\ &= \left|H^{(1,2)}_m(\alpha)\right|^2 = \tfrac{1}{4}\left|G^D_{m,A}(\alpha)\right|^2.\end{aligned} \tag{5.4}$$

We can thus proceed with $\partial_{\log}\left[G^D_{m,A}(\alpha)\right]$ as follows.

$$\begin{aligned}&\Gamma(\alpha)\partial_{\log}\left[G^D_{m,A}(\alpha)\right] \\ &= \frac{dJ_m(\alpha)}{d\alpha} J_m(\alpha) + |A|^2 \frac{dY_m(\alpha)}{d\alpha} Y_m(\alpha) \\ &\quad + A_i\left[\frac{dJ_m(\alpha)}{d\alpha} Y_m(\alpha) + \frac{dY_m(\alpha)}{d\alpha} J_m(\alpha)\right] \cdot \\ &\quad + iA_r\left[\frac{dJ_m(\alpha)}{d\alpha} Y_m(\alpha) - \frac{dY_m(\alpha)}{d\alpha} J_m(\alpha)\right]\end{aligned} \tag{5.5}$$

As $\mathrm{Im}\left\{\partial_{\log}\left[G^D_{m,A}(\alpha)\right]\right\}$ is needed for Eq. (5.1), the two leading rows in the above Eq. (5.5) do not make any contributions. We are thus left with the last row of Eq. (5.5).

$$\begin{aligned}&\mathrm{Im}\left\{\partial_{\log}\left[G^D_{m,A}(\alpha)\right]\right\}/A_r \\ &= \frac{dJ_m(\alpha)}{d\alpha} Y_m(\alpha) - \frac{dY_m(\alpha)}{d\alpha} J_m(\alpha) \\ &= -\frac{2}{\pi\alpha}\end{aligned} \tag{5.6}$$

Here, we utilized the Wronskian formula between $J_m(\alpha)$ and $Y_m(\alpha)$ [2].

Reverting to $\alpha \equiv q\rho$, we obtain the following desired formula for (5.1) [4].

$$P^D_r = -\frac{2}{\pi q\rho} A_r \frac{\left|H^D_z(q\rho)\right|^2}{\Gamma(q\rho)} \propto -\frac{A_r}{q\rho}. \tag{5.7}$$

Here, a use is made of Eq. (5.4). Now, two key facts can be observed from Eq. (5.7). Firstly, $P^D_r < 0$ if $A_r > 0$, thereby denoting a net inward energy flow in the radial direction. Indeed, all the numerical data presented in Fig. 3 indicates $A_r > 0$. Physically speaking, a net energy should be rushed radially inward in order to compensate for the energy dissipation by metals in the cylindrical interior. Secondly, the circumferentially integrated energy flow $\rho P^D_r(\rho q)$ remains constant since $\rho P^D_r(\rho q) \propto -A_r/q$ as seen from Eq. (5.7) [33].

For numerical computations, the profile of $H^D_z$ given in Eq. (2.7) is employed. For simplicity, field values at $\rho = 1_+$ on the dielectric side of the M-D interface are evaluated to provide both $P^D_{\theta,R+}$ and $P^D_{r,R+}$. Therefore, the vector $\vec{P}^D_{R+} = P^D_{r,R+}\hat{e}_r + P^D_{\theta,R+}\hat{e}_\theta$ is formed with $(\hat{e}_r, \hat{e}_\theta)$ being the unit vectors along the $(r, \theta)$ -coordinates.

Figure 5(a) plots scaled vector $\vec{P}^D_{R+} \equiv P^D_{r,R+}\hat{e}_r + P^D_{\theta,R+}\hat{e}_\theta$ as $m$ is varied over $m = 0,1,\cdots,9,10$. Notice for the two components that $P^D_{r,R+} < 0$ for all $m$, whereas $P^D_{\theta,R+} > 0$. Figure 5(b) shows a typical scattering situation, which involves both incoming and outgoing waves represented respectively by $H^{(2)}_m$ and $H^{(1)}_m$ [9, 37]. According to, say, the red bar with $m = 2$ in Fig. 5(a) for $\vec{P}^D_{R+}$, the reflection is not specular (namely, the reflection angle being different from the incidence angle) due to metallic loss as displayed in Fig. 5(b).

Notice that $\left|H^D_z(q=1)\right| = 1$ by definition in Eq. (2.7). Hence, Eq. (5.1) shows that the condition $P^D_{r,R+} < 0$ is

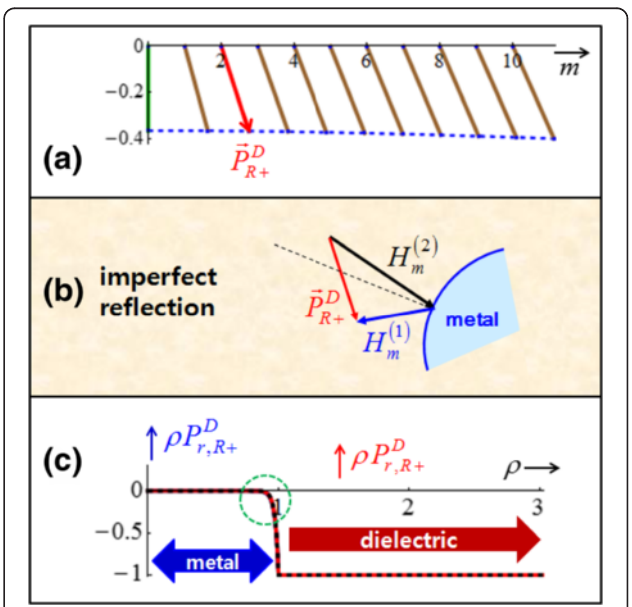


**Fig. 5** **a** The Poynting vector $\vec{P}^D_{R+} \equiv P^D_{r,R+}\hat{e}_r + P^D_{\theta,R+}\hat{e}_\theta$ on the cross-sectional plane evaluated at $\rho = 1_+$ with increasing $0 \le m \in \mathbb{Z}$. **b** An imperfect reflection of an outgoing wave for a given incoming wave. **c** The radial profile of the circumferentially integrated $\rho P^D_r(\rho)$

identical to $P^D_{r,R+} = \mathrm{Im}(\mathcal{R}_D) < 0$ , where $\mathcal{R}_D \equiv \partial_{\log}\left[G^D_{m,A}(q)\right]$ from Eq. (2.12). As a result, $\mathrm{Im}(\mathcal{R}_M) < 0$ in the interior from the dispersion relation $\mathcal{R}_M = \mathcal{R}_D$ in Eq. (2.10). Similarly, $P^M_r(\rho)$ can be computed.

Let us rescale both $P^{M,D}_r(\rho)$ such that $P^{M,D}_r(\rho)/P^{M,D}_r(\rho = 1) \to P^{M,D}_r(\rho)$ . On this new scale, $P^{M,D}_r(1) = 1$ . Figure 5(c) displays the circumferentially integrated $\rho P^{M,D}_r(\rho)$, where the additional constant factor $2\pi k_0 R$ is neglected. Therefore, $\rho P^D_r(\rho) = 1$ for all $1 \le \rho < \infty$ in Fig. 5(c) [33]. The single-curve-like black-red dotted curves result from an almost complete overlap for the five curves drawn for $m = 0,2,4,6,8$. However, there do exist finite non-zero differences among the various profiles, especially on the metallic side in the vicinity of the M-D interface as marked by a green broken circle in Fig. 5(c). This field confinement accompanied by a penetration feature [4, 10, 17, 28, 29] is similar to the boundary-layer feature in fluid dynamics [19].

## 6. Light spins and upper bounds

Consider the light spin vector $\vec{S} = (S_r, S_\theta, S_z)$ defined as follows [6, 7, 22, 24].

$$\vec{S} \equiv \frac{g}{2}\mathrm{Im}\left(|\varepsilon|\vec{E}^{\,*} \times \vec{E} + \vec{H}^{\,*} \times \vec{H}\right). \tag{6.1}$$

Here, $g$ is a constant depending on the system of units. Notice that $\vec{S}$ comes in dual terms by consisting of both electric and magnetic parts [7, 32]. In terms of light-particle interactions [7], light spins are related to the torque exerted on particles by light.

Because of the single non-zero magnetic field $H_z$, the term $\mathrm{Im}\left(\vec{H}^{\,*} \times \vec{H}\right)$ vanishes identically. Since non-zero electric field components ($E_r$, $E_\theta$) lie on the cross-sectional plane, $\left(\vec{E}^{\,*} \times \vec{E}\right)_z = E^*_r E_\theta - E^*_\theta E_r$, whereas $S_r = S_\theta = 0$ identically. As a result, $\mathrm{Im}\left(\vec{E}^{\,*} \times \vec{E}\right)_z = 2\mathrm{Im}\left(E^*_r E_\theta\right)$ so that the sole non-zero spin component is given by.

$$S_z \equiv g|\varepsilon|\mathrm{Im}\left(E^*_r E_\theta\right). \tag{6.2}$$

On the other hand, the electromagnetic energy density $W$ is defined as follows also in dual terms [7, 15, 24].

$$W = \frac{g\omega}{2}\left(|\varepsilon|\left\|\vec{E}\right\|^2 + \left\|\vec{H}\right\|^2\right). \tag{6.3}$$

Here, the factor $|\varepsilon|$ in the term $|\varepsilon|\left\|\vec{E}\right\|^2$ accounts for the positivity of energy [40].

As $\left\|\vec{E}\right\|^2 = \vec{E}^{\,*} \cdot \vec{E} = |E_r|^2 + |E_\theta|^2$ and $\left\|\vec{H}\right\|^2 = |H_z|^2$ for our particular cylindrical wave,

$$W = \frac{g\omega}{2}\left[|\varepsilon|\left(|E_r|^2 + |E_\theta|^2\right) + |H_z|^2\right]. \tag{6.4}$$

In the meantime, the specific transverse light spin $s_z$ (to be henceforth shortened as "specific spin") in the axial $z$-direction is defined with respect to energy density of electromagnetic waves [7, 24].

$$s_z \equiv \frac{\omega S_z}{W} = \frac{2|\varepsilon|\mathrm{Im}\left(E^*_r E_\theta\right)}{|\varepsilon|\left(|E_r|^2 + |E_\theta|^2\right) + |H_z|^2}. \tag{6.5}$$

We can prove that its magnitude is bounded such that $|s_z| \le 1$ without actually plugging the solutions ($E_r$, $E_\theta$, $H_z$) related via Eq. (2.3) into Eqs. (6.2) and (6.4). This requires only an invocation of Cauchy-Schwarz inequality $\mathrm{Im}\left(E^*_r E_\theta\right) \le |E_r||E_\theta|$ in Eq. (1.2) as follows.

$$|s_z| \le \frac{2|\varepsilon||E_r||E_\theta|}{|\varepsilon|\left(|E_r|^2 + |E_\theta|^2\right) + |H_z|^2}. \tag{6.6}$$

Hence,

$$\begin{aligned} &1 - |s_z| \ge \frac{N_{spin}}{D_{spin}} \\ &D_{spin} \equiv |\varepsilon|\left(|E_r|^2 + |E_\theta|^2\right) + |H_z|^2 \\ &N_{spin} \equiv |\varepsilon|\left(|E_r|^2 + |E_\theta|^2\right) + |H_z|^2 - 2|\varepsilon||E_r||E_\theta| \\ &\quad = |\varepsilon|\left(|E_r| - |E_\theta|\right)^2 + |H_z|^2 \ge 0 \end{aligned} . \tag{6.7}$$

Consequently, $|s_z| \le 1$ is proved. In addition, we expect that $|s_z| = 1$ hardly occurs, because of the positive term $|H_z|^2$ in the definition for $N_{spin}$ of the above equation. Therefore, the only chance that $|s_z| \to 1$ is feasible occurs in two cases: (1) as $|E_r|, |E_\theta|, |H_z| \to 0$, viz., or (2) as $|E_r| = |E_\theta|$ and $|H_z| \to 0$. Both cases can be called an optical singularity [5]. Via the upcoming Eqs. (6.12) and (6.13), we will find that the latter case (2) is the correct one. This point will become clear from the forthcoming Figs. 5 and 7 obtained through numerical computations.

Via Maxwell's equations, we can numerically evaluate the specific spin $s_z \equiv \omega S_z / W$ in Eq. (6.5). To this end, both $\varepsilon$ and $\vec{E}$ should be specialized to $\varepsilon_{M,D}$ and $\vec{E}^{\,M,D}$ whenever need arises. By following the steps similar to Eqs. (5.1)-(5.7), we can arrive at the analytic expression for $S^{M,D}_z$ from Eqs. (2.3) and (2.7).

$$\begin{cases} S_z^M = 2\dfrac{m}{|\varepsilon_M|}\dfrac{|H_z^M|^2}{k_0 R\rho}\mathrm{Re}\left\{\sqrt{\varepsilon_M}\partial_{\log}[J_m(\sqrt{\varepsilon_M}q\rho)]\right\} \\ S_z^D = 2m\dfrac{|H_z^D|^2}{k_0 R\rho}\mathrm{Re}\left\{\partial_{\log}\left[G_{m,A}^D(q\rho)\right]\right\} \end{cases}. \tag{6.8}$$

By comparing Eq. (5.1) with Eq. (2.7) to Eq. (6.8), $(P_r^D, S_z^D)$ turns out to form a complex-conjugate pair through the common factor $\partial_{\log}\left[G_{m,A}^D(q\rho)\right]$. However, $S_z^D$ is related to $P_\theta^D = m(\rho q)^{-1}|H_z^D|^2$ through $m$ as well.

Figure 6 plots the specific spins $s_z^{M,D}$ in both interior and exterior. Because the specific spin vanishes for non-rotational waves defined with $m = 0$, only cases with $m = 1,2,3,\cdots$ are considered. For simplicity, only four cases with $m = 1,2,4,10$ are presented here. Let us present three items of findings from Fig. 6.

Firstly, we find from Fig. 6 that $|s_z^{M,D}| \le 1$ as has already been proved in Eq. (6.7). In the exterior, $s_z^D$ undergoes sinusoidal undulations between up-spins with $s_z^D > 0$ and down-spins with $s_z^D < 0$. Since $\varepsilon_M = -8.93 + 0.979i \in \mathbb{C}$, the metal in the cylindrical interior is analogous to a viscous fluid. In contrast, the surrounding dielectric (vacuum) with $\varepsilon_D = 1$ can be thought of as an inviscid fluid [19].

In fact, Maxwell's equations in Eq. (2.1) possess characteristics pertaining to a system of parabolic PDEs because $\varepsilon_M \in \mathbb{C}$ with $\mathrm{Im}(\varepsilon_M) > 0$, although they are apparently a system of hyperbolic PDEs [4, 40]. See [20] for full discussions. From this perspective, the monotonic profile in the metallic interior shown in Fig. 6 is analogous to what we find with a fluid of a larger viscosity. In comparison, the oscillatory feature shown in the dielectric exterior is what we encounter with a fluid of a smaller viscosity.

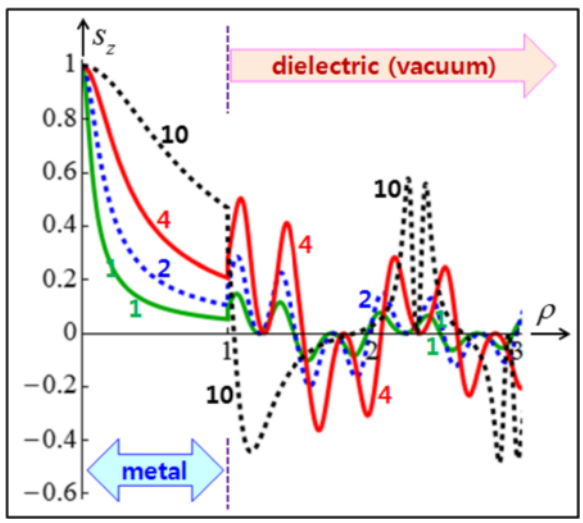


**Fig. 6** The radial profile of the specific spin $s_z(\rho)$ over the range $0 \le \rho \le 3$. Four curves are generated for $m = 1,2,4,10$ in different colors

Secondly, $s_z^M \to 1$ as $\rho \to 0$ or $r \to 0$, regardless of $m > 0$. This fact appears a bit contradictory to Eq. (6.8), which seemingly predicts $s_z^M \propto m$. In order to resolve this contraction, let us specialize $s_z \equiv \omega S_z / W$ in Eq. (6.5) to $s_z^M \equiv \omega S_z^M / W_M$ in the metallic interior.

$$s_z^M = \frac{|\varepsilon_M|\mathrm{Im}\left[(E_r^M)^* E_\theta^M\right]}{|\varepsilon_M|\left(|E_r^M|^2 + |E_\theta^M|^2\right) + |H_z^M|^2}. \tag{6.9}$$

Here, we specialized both Eq. (6.2) to $S_z^M$ and Eq. (6.4) to $W_M$. Furthermore, Eq. (2.3) is specialized to $E_r^M$ and $E_\theta^M$, respectively.

When both $E_r^M$ and $E_\theta^M$ from Eq. (2.3) are plugged into Eq. (6.9),

$$s_z^M = \frac{2\mathrm{Im}\left[i\frac{m}{k_0 r}\left(H_z^M\right)^* \frac{1}{k_0}\frac{dH_z^M}{dr}\right]}{\left(\left|\frac{m}{k_0 r}H_z^M\right|^2 + \left|\frac{1}{k_0}\frac{dH_z^M}{dr}\right|^2\right) + |\varepsilon_M||H_z^M|^2}. \tag{6.10}$$

Notice that $k_0 r \equiv \rho q$ is dimensionless from $q \equiv k_0 R$ and $\rho \equiv r/R$. Since both numerator and denominator of Eq. (6.10) are homogeneous in $H_z^M$, we can set $H_z^M = J_m(\sqrt{\varepsilon_M}q\rho)$ instead of the normalized $H_z^M = J_m(\sqrt{\varepsilon_M}q\rho)/J_m(\sqrt{\varepsilon_M}q)$ in Eq. (2.7). It is because $J_m(\sqrt{\varepsilon_M}q)$ is just a normalization constant in view of varying $\rho$.

The desired proof that $s_z^M \to 1$ as $\rho \to 0$ can be rather easily ascertained by the asymptotic formula that $J_m(\alpha) \to (m!)^{-1}(\alpha/2)^m$ as $|\alpha| \to 0$ for $\alpha \in \mathbb{C}$ [2]. Notice that $\sqrt{\varepsilon_M}\rho q \in \mathbb{C}$ in the argument of $J_m(\sqrt{\varepsilon_M}\rho q)$, although $\rho, q \in \mathbb{R}$. Now, Eq. (6.10) is examined as $\rho \to 0$ as follows.

$$s_z^M = \frac{2\mathrm{Re}\left[\frac{m}{q\rho}(\rho^m)^* \frac{1}{q}\frac{d\rho^m}{d\rho}\right]}{\left(\left|\frac{m}{q\rho}\rho^m\right|^2 + \left|\frac{1}{q}\frac{d\rho^m}{d\rho}\right|^2\right) + |\varepsilon_M||\rho^m|^2}. \tag{6.11}$$

Here, we implemented $\mathrm{Im}(i\alpha) = \mathrm{Re}(\alpha)$ for $\alpha \in \mathbb{C}$ in arriving from Eq. (6.10) at Eq. (6.11).

In addition, the common factor $|\varepsilon_M|(2^m m!)^{-2}q^2$ has been canceled during this step. Simplifying further,

$$s_z^M = \frac{2\frac{m^2}{q^2}\rho^{2m-2}}{\frac{m^2}{q^2}\rho^{2m-2} + \frac{m^2}{q^2}\rho^{2m-2} + |\varepsilon_M|\rho^{2m}}. \tag{6.12}$$

The last term in the denominator is much smaller than the two leading terms, since $\rho^{2m} << \rho^{2m-2}$ as $\rho \to 0$. In

other words, the axial transverse magnetic-field component $H_z^M$ makes a negligible contribution to the energy density in comparison to both $E_r^M$ and $E_\theta^M$ as $\rho \to 0$. In comparison, both cross-sectional electric-field components $E_r^M$ and $E_\theta^M$ make an equal contribution to the energy density $W$ as $\rho \to 0$. In terms of Cartesian coordinates, both $E_x^M$ and $E_y^M$ make an equal contribution to the energy density in Eq. (6.4). In other words, perfect circular polarization prevails as $\rho \to 0$, thereby being a symptom of optical singularity [5, 21, 32].

Therefore, it is proved that $s_z^M \to 1$ as $\rho \to 0$. This point can be understood alternatively from Eq. (6.6) as follows

$$|s_z| \to \frac{2|\varepsilon||E_r||E_r|}{|\varepsilon|\left(|E_r|^2 + |E_r|^2\right)} = 1 \quad \because \begin{pmatrix} |E_r| \to |E_\theta| \\ |H_z| \to 0 \end{pmatrix} \quad as \quad \rho \to 0 \qquad (6.13)$$

Thirdly, $s_z^M \neq s_z^D$ across the M-D interface, which is relevant to the spin-orbital interaction taking place across material interfaces [7, 38]. This jump in the specific spin can be understood again in terms of the analogy to fluid dynamics. In other word, there should be a sudden jump across an interface from the side of a larger-viscosity fluid to the side of a smaller-viscosity fluid [20].

However, there exist sign changes in $s_z^M - s_z^D$ as $m$ is varied. The reason is that our three interface conditions of $\varepsilon_M E_r^M = \varepsilon_D E_r^D$, $E_\theta^M = E_\theta^D$, and $H_z^M = H_z^D$ cannot be directly translated into the traditional fluid dynamic interface conditions. In this regard, the fluid dynamic conditions between a solid and an adjoining fluid may be either perfectly sticky adherence or no slips [19].

Figure 7 shows the jump in the specific spin $\Delta s_z \equiv s_z^D(\rho = 1_+) - s_z^M(\rho = 1_-)$ across the metal-dielectric (M-D) interface. The angular mode index $m$ is increased in Fig. 7(a) over $m = 1,2,\cdots,19,20$ in increments of one, whereas it is increased in Fig. 7(b) over $m = 21,23,\cdots,53,55$ in increments of two. It seems that $\Delta s_z > 0$ only for the lower angular speeds with $m = 1,2,\cdots,5,6$. In special, the maximum in $\Delta s_z$ takes place for $m = 3$. On the other hand, $\Delta s_z < 0$ for $m \geq 7$, whereas its magnitude $|\Delta s_z|$ appears to approach a certain limit value as $m \to \infty$ as inferred from Fig. 7(b). This trend should be associated with the limit behavior in Fig. 3 that $A \to 0$ as $m \to \infty$. We have not attempted its analytic proof, but we believe that it can be performed. In addition, this jump is related to spin-orbital interactions [7, 38].

## 7. Polarization and two-dimensionality

In polar coordinates, consider a second-order degree of polarization (DOP) $\Pi_{r\theta,2}$ for the electric-field components on the cross-sectional plane [41].

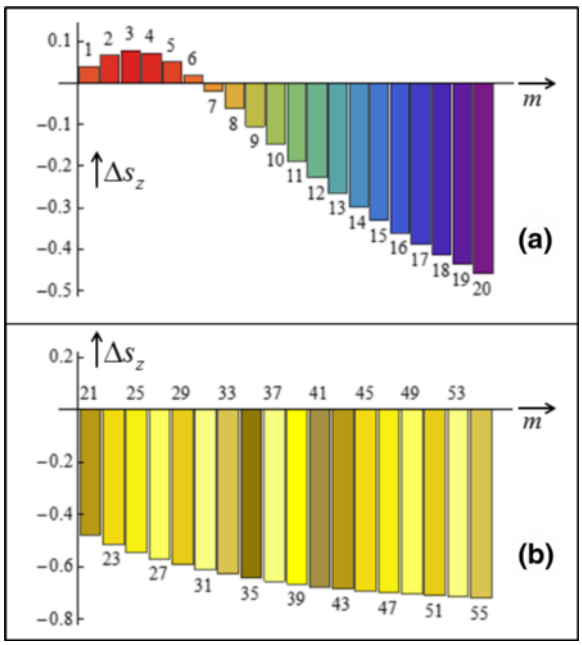


**Fig. 7** The jump in the specific spin $\Delta s_z \equiv s_z^D(\rho = 1_+) - s_z^M(\rho = 1_-)$ across the metal-dielectric interface as $m$ is increased **a** for smaller $m$'s and **b** for larger $m$'s

$$\Pi_{r\theta,2} \equiv \frac{|E_r|^2 - |E_\theta|^2}{|E_r|^2 + |E_\theta|^2}. \qquad (7.1)$$

Therefore, $\Pi_{r\theta,2} = 1$ and $\Pi_{r\theta,2} = -1$ refer respectively to the pure radial and angular polarizations. On the other hand, $\Pi_{r\theta,2} = 0$ refers to the perfect circular polarization. Traditionally, $\Pi_{r\theta,2}$ has been called the in-plane polarization [7].

Figure 8 shows $\Pi_{r\theta,2}$ for the four values of $m = 1, 2, 4, 10$. Figure 8 looks quite similar to that of the specific spin $s_z$ in Fig. 6. Of course, the optical vortices can be seen where $s_z \to 1$ in Fig. 6 and where $\Pi_{r\theta,2} \to 0$ in Fig. 8 both as $\rho \to 0$ [5, 21]. Here, a phase singularity takes place and a perfect circular polarization applies as summarized in Eq. (6.13).

However, upon closer look at both figures, the locations where $s_z = 0$ in Fig. 6 are irregularly spaced, whereas the locations where $\Pi_{r\theta,2} = 0$ in Fig. 8 are rather regularly spaced. Those locations are of course do not coincide. Therefore, $s_z$ and $\Pi_{r\theta,2}$ are certainly unequal, thereby negating the traditional notion that the electric-field polarization is the same as the light (specific) spin.

Prompted by the upper bound on $|s_z|$ defined through both Eqs. (6.6) and (6.7), we introduce two additional degrees of polarization $\Pi_{r\theta,1}$ and $\Pi_{r\theta z}$.

$$\Pi_{r\theta,1} \equiv \frac{|E_r| - |E_\theta|}{|E_r| + |E_\theta|}. \qquad (7.2)$$

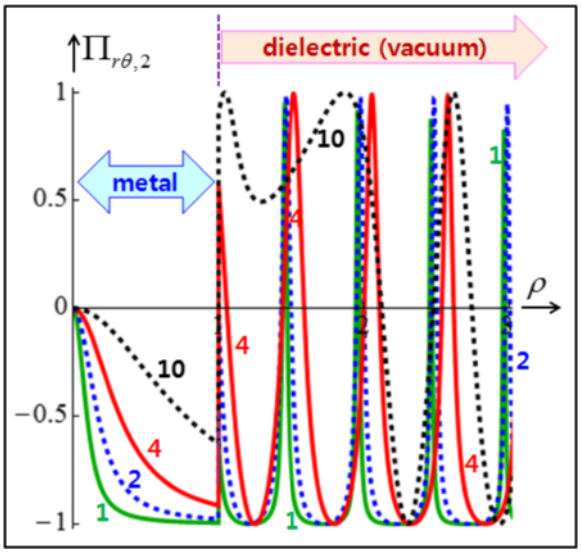


**Fig. 8** The radial profile of the second-order degree of polarization in the polar coordinate $\Pi_{r\theta,2}$ for the four values of $m = 1,2,4,10$

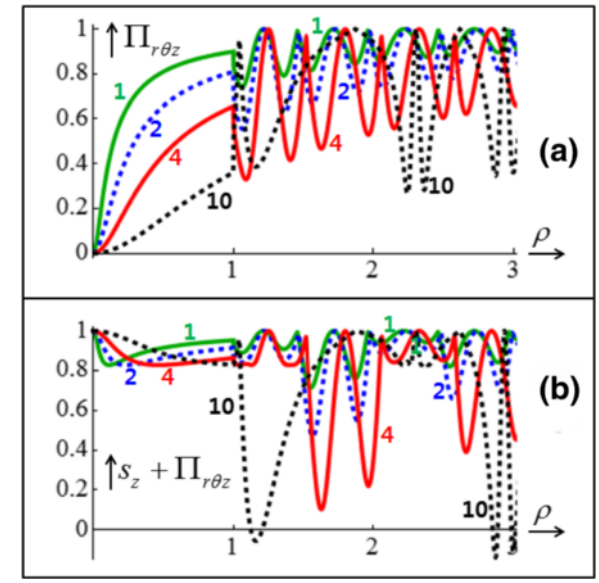


**Fig. 9 a** The radial profile of the vectorial degree of polarization in the polar coordinate $\Pi_{r\theta z}$ for the four values of $m = 1, 2, 4, 10$. **b** The profile for $s_z + \Pi_{r\theta z}$

$$\Pi_{r\theta z} \equiv \frac{|\varepsilon|(|E_r|-|E_\theta|)^2 + |H_z|^2}{|\varepsilon|(|E_r|+|E_\theta|)^2 + |H_z|^2}. \tag{7.3}$$

Here, $\Pi_{r\theta,1}$ is a first-order DOP, in comparison to the second-order one $\Pi_{r\theta,2}$ previously defined in Eq. (7.1).

As a result, the vectorial DOP $\Pi_{r\theta z}$ is an extended form of $\Pi_{r\theta,1}$ by accounting for the vectorial nature of the total field ($E_r$, $E_\theta$, $H_z$) of our TM wave. Of course, $\Pi_{r\theta z}$ contains the weighting actor $\sqrt{|\varepsilon|}$ for both $E_r$ and $E_\theta$ in comparison to one (for our non-magnetic media with $\sqrt{\mu} = 1$) for $H_z$. The bound on the specific spin in Eq. (6.7) now reads as follows.

$$|s_z| + \Pi_{r\theta z} \le 1. \tag{7.4}$$

Figure 9(a) presents the radial profile of $\Pi_{r\theta z}$ for the four values of $m = 1,2,4,10$. We find that $\Pi_{r\theta z}$ in Fig. 9(a) looks like something in between $|s_z|$ in Fig. 6 and $\Pi_{r\theta,2}$ in Fig. 8. Meanwhile, Fig. 9(b) displays the radial profile of the sum $s_z + \Pi_{r\theta z}$, thus exhibiting the sharpness of the upper bound in Eq. (7.4).

Through the coordinate transforms $E_x = E_r \cos\theta - E_\theta \sin\theta$ and $E_y = E_r \sin\theta + E_\theta \cos\theta$, $\Pi_{r\theta,2}$ in Eq. (7.1) can be transformed into the following DOP $\Pi_{xy}$ in the Cartesian coordinates.

$$\Pi_{xy} \equiv \frac{|E_x|^2 - |E_y|^2}{|E_x|^2 + |E_y|^2}. \tag{7.5}$$

Figure 10 shows $\Pi_{xy}$ on the cross-sectional plane of a nanowire for $m = 4,10$. Here, $\xi \equiv x/R$ and $\eta \equiv y/R$, and hence $\xi^2 + \eta^2 = \rho^2$. The white horizontal and vertical lines indicate respectively $\eta = 0$ and $\xi = 0$. The more reddish and bluish colors correspond respectively to larger and smaller values of $\Pi_{xy}$. Hence, the color change corresponds to the circular polarization. The strongest red color corresponds to $\Pi_{xy} = 1$ for the $x$-polarized electric field, whereas the strongest blue color corresponds to $\Pi_{xy} = -1$ for the $y$-polarized electric field.

A common feature of both panels in Fig. 10 is that the interior exhibits a rather monotone trend in the radial direction. This is consistent with both Figs. 6 and 8 with a similar monotonic evanescent feature in the interior [8, 32]. In comparison, the exterior reveals characteristic sinusoidal undulations again as in Figs. 6 and 8. Another common feature in Fig. 10 is that the whole $\Pi_{xy}$ -pattern is twice periodic in the angular direction due to $\cos(2\theta)$ and $\sin(2\theta)$.

Let us tell the difference between the two panels of Fig. 10. To this end, a red broken line is drawn on each panel on the first quadrant. It is thus found that the angle subtended by this broken slant line and the horizontal axis is visibly less than 45° in Fig. 10(a) for $m = 4$, whereas it is almost 45° in Fig. 10(b) for $m = 10$. Therefore, the rotational strength alters the handedness of circular polarization characteristics to some degrees.

## 8. Angular-mode dynamics

Michael Berry [4] suggested in 1975 a necessity of taking the incoming energy absorption into account in his treatment of gently curved bends, for which he suggested $m \in \mathbb{R}$ as well. Since then, curved surfaces have attracted researchers involved in waveguides design [14, 26]. We

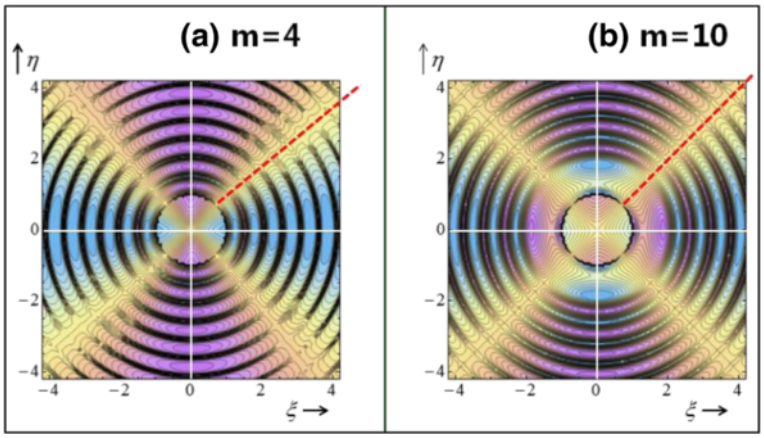


**Fig. 10** Degree of electric-field polarization $\Pi_{xy}(\xi, \eta)$ in Cartesian coordinates for $m = 4, 10$

employed a commercial software Mathematica® so that there is no constraint on $m$. Hence, $m$ is relaxed to take real values, viz., $0 \le m \in \mathbb{R}$. In this way, a continuous transition in $A(m)$ is obtained, which we call "angular-mode dynamics. See Fig. 3 for reference.

Figure 11 displays one of such curves, for instance, over the range $1.613 \le m \le 3.1$. To this goal, ten of $m$'s are prepared according to $m_j = (0.93)^j m_0$ with $j = 1,2,\cdots,9$. With the starting $m_0 = 3.1$, the trailing $m_9 = 1.613$ is obtained. Different colors are assigned to the dots with the head in red and the tail in blue so that a comet-like dot chain is constructed.

Based on the same technique employed for drawing Fig. 11, Additional file 1 is generated by increasing the starting $m_0$, but with a slightly different scaling. Let us briefly explain how Additional file 1 is constructed. After its inception with $m_0 = 0$ below the axis at $\bar{A}_i = 0$, a comet with increasing $m_0$ appears to make three turns (two across the $\bar{A}_i = 0$ -line, and one below it) before approaching the origin. In general, it is found from Fig. 11(a) that there is an abrupt stepping over the line at $\bar{A}_i = 0$. With $m = 20$, the small Fig. 11(b) is prepared on the lower right corner of Fig. 11(a).

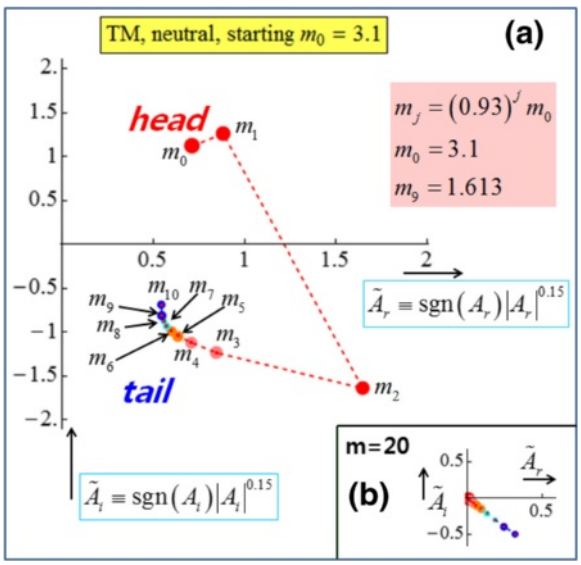


**Fig. 11** The scaled asymmetry parameter $\bar{A}$ with successively varying $0 \le m \in \mathbb{R}$ **a** with the starting $m_0 = 3.1$, and **b** with the starting $m_0 = 20$. Here, $\bar{A}_r \equiv \mathrm{sgn}(A_r)|A_r|^{0.15}$ and similarly for $\bar{A}_i$

It is found from Fig. 11(b) that $\bar{A} \to 0$ or $A \to 0$, thus signifying an equal importance of both incoming and outgoing waves. From further numerical computations we confirmed that $\bar{A} \to 0$ or $A \to 0$ as $m \to \infty$. It is because large rotations render relatively insignificant the difference between the two types of waves in vacuum. This limit behavior is related to the limit behavior of the spin jump $\Delta s_z$ as $m \to \infty$ in Fig. 7(b).

Both from a closer counting on Fig. 3 and from Additional file 1 we find that the crossings over $\bar{A}_i = 0$ take place only between the four pairs of integer $m$'s: (0,1), (1,2), (2,3), and (4,5). In special, no crossing occurs for the pair (3,4). Obviously, there are no more crossings after $m = 5$ either. The crossing condition is equivalent to $A_i = 0$ by definition, for which we computed the four roots for the pairs of $(m, A_r)$:

$$\begin{cases} (0.341, 61.7) \\ (1.44, 0.0167) \\ (2.70, 54.5) \\ (4.26, 0.0229) \end{cases}. \tag{8.1}$$

All these pairs do not refer to realistic neutral states, because of the non-integer $m$. Recall that a non-integer $m$ refers at most to curved bends or partial arcs, because it does not satisfy angular periodicity.

Take the pair $(m, A_r) = (2.69683, 54.5273)$ in Eq. (8.1) as an example, which is accurate to within six valid

digits. Its value $A_r = 54.5273$ lies by far margin off the range $0 \le A_r \le 2$, which is employed for Fig. 11 and all the frames of Additional file 1. We tried hard to capture this state by successively drawing more frames around $m = 2.69683$ as seen from Additional file 1. These trials were not quite successful, thereby ushering us to a belief that the crossing between $2< m <3$ is really wild one. As a result, we can infer both rareness and eventfulness of our rotationally propagating waves with integer angular mode indices.

We emphasize that our whole purpose of displaying the angular-mode dynamics with $0 \le m \in \mathbb{R}$ as shown in Fig. 11 and Additional file 1 is not to claim that $m \in \mathbb{R}$ are valid physical values. Instead, we reaffirm that $m \in \mathbb{Z}$ employed in separating given PDEs into ODEs is really the correct one in conformity to the angular periodicity. In other words, the discreteness represented by $m \in \mathbb{Z}$ refers to rare and possibly stable events instead of the possibly unstable continuum represented by $m \in \mathbb{R}$. We suppose that a pertinent stability analysis will require a separate study.

## 9. Discussions

In the latter part of Section 2, a set of simple analysis and computations has been carried out for lossless metals with $\varepsilon_M = -8.93$, viz., with $\mathrm{Im}(\varepsilon_M) = 0$. Compare this to our standard data in Eq. (2.6). In case with $\varepsilon_M = -8.93$, the radial Poynting component vanishes throughout, namely, $P_r^{M,D}(\rho) = 0$ for all $0 \le \rho < \infty$. In conformity to Eq. (5.7), we found numerically that $A_r = 0$ and $A_i \ne 0$. Therefore, both incoming and outgoing waves are of the same magnitude, but they are of different phases. In addition, light spins are identically zero, including $S_z = 0$. Therefore, most of the non-trivial results shown in this study are indeed loss-induced due to $\mathrm{Im}(\varepsilon_M) \ne 0$, while being gain-compensated.

Another issue as regards plasmonic waves arises from $\varepsilon_M \in \mathbb{C}$, where $\mathrm{Im}(\varepsilon_M)$ incurs energy dissipation due to lossy metals. This causes a great difficulty in constructing a proper formula for energy density via, for instance, terms like $\varepsilon_M \left(\vec{E}^M\right)^* \cdot \vec{E}^M \equiv \varepsilon_M \left\|\vec{E}^M\right\|^2$. Here, both subscript and superscript mean "metals". It is obvious that $\varepsilon_M \left\|\vec{E}^M\right\|^2$ cannot make up an energy content since $\varepsilon_M \left\|\vec{E}^M\right\|^2 \in \mathbb{C}$. For lossless dielectric media such as vacuum with $\varepsilon_D > 0$, $\varepsilon_D \left\|\vec{E}^D\right\|^2 > 0$, thereby causing no problem at all [6, 7, 24]. In general, formulating a proper energy density for lossy media has been a headache. In this aspect, our remedy in this study was to handle $\vec{E}$ with a multiplying factor $\sqrt{|\varepsilon|} > 0$ for any media with $\varepsilon \in \mathbb{C}$. This product $\sqrt{|\varepsilon|}\,\vec{E}$ works very well in Eqs. (6.1) and (6.3). Even the modified Poynting vector $\vec{P} \equiv \sqrt{|\varepsilon|}\mathrm{Re}\left(\vec{E} \times \vec{H}^*\right)$ worked fine in terms of dimensionality. In particular, the directions of energy flows are preserved since the original unmodified formula is $\vec{P} \equiv \mathrm{Re}\left(\vec{E} \times \vec{H}^*\right)$.

Processing Maxwell equations with the non-zero field components ($E_r$, $E_\theta$, $H_z$) for our TM wave, we came up with non-zero Poynting components and light spin ($P_r$, $P_\theta$, $S_z$). The complex-conjugate relationship between ($S_z$, $P_r$) stands in a similarity to $x + iy \equiv r\exp(i\theta)$ valid between the cross-sectional Cartesian coordinates ($x$, $y$) and the polar coordinates ($r$, $\theta$). We believe that these different pairings would impact on the incipience of axial waves when starting from the purely cross-sectional planar waves [9]. As an additional comment, spatially global characteristics such as global specific spins and various global polarizations can be evaluated, but mostly by numerical integrations over the radial range [24].

Let us examine the implications of the two-dimensionality, where all the field components depend only on the cross-sectional coordinates ($r$, $\theta$). The pair ($H_z$, $S_z$) of out-of-plane components is typical of the strong effects exerted by an axial magnetic field on the light spin [6, 7, 18]. This interaction between $H_z$ and $S_z$ is the key ingredient of topological photonics, where mathematical curiosity unfolds itself with an accelerating pace in these days [32].

This topological nature is related to the fact that our cylindrical waves are described in terms of only two space coordinates. In this regard, notice even in the absence of metallic loss that wave diffusion takes place not in three- but in two-dimensional space, albeit in unbounded domains [16, 40]. In contrast, Huygens principle holds true not in two- but in three-dimensional space according to Kirchhoff's formula [31, 40]. Therefore, the residual effect due to wave diffusion could be mixed up with the residual effect caused by metallic loss in two-dimensional configurations such as ours.

It is amusing to draw another analogy between our cylindrical waves and people living on a flat land [1]. To this end, let us regard both $E_r$ and $E_\theta$ as two kinds of people confined to the cross-sectional plane. Both are assumed to move only on this flat land with their respective magnitudes and phases. The only way both kinds of people can communicate with each other is by the transverse axial component $H_z$ through Eq. (2.3). Here, $H_z$ is considered to possess its magnitude and phase not on the cross-sectional plane but along the out-of-plane axial direction. In this sense, people on our

flat land are not wholly confined to the flatland, but they have communication channels via three-dimensional space.

Let us tell how we became motivated to examine the current problem. By this way, we hope to pose an open (mathematical) problem. To this goal, consider a coherent combination of the transverse-electric (TE) wave with its non-zero field components ($H_r$, $H_\theta$, $E_z$) and the transverse-magnetic (TM) wave with its non-zero field components ($E_r$, $E_\theta$, $H_z$) [7, 9, 17, 32, 36]. Notice that TM and TE waves are oppositely defined in some literature [11, 16, 32].

Instead of the pair of the electric field $\vec{E}$ and the magnetic field $\vec{H}$, consider a pair of two generic vectors $\vec{A}$ and $\vec{B}$ in three-dimensional space. In other words, $\vec{A}, \vec{B} \in \Re^3$ or $\vec{A} \equiv (A_x, A_y, A_z)$ and $\vec{B} \equiv (B_x, B_y, B_z)$ in Cartesian coordinates respectively in component forms. The combined energy is then written to be

$$W_{AB} \equiv \frac{1}{2}\left(\left\|\vec{A}\right\|^2 + \left\|\vec{B}\right\|^2\right). \tag{9.1}$$

Among possible quantities characterizing such a pair of vector fields [30, 35]., a generalized spin vector $\vec{S}_{AB}$ is defined accordingly by $\vec{S}_{AB} \equiv (1/2)\mathrm{Im}\left(\vec{A}^* \times \vec{A} + \vec{B}^* \times \vec{B}\right)$ with $\vec{S}_{AB} \in \mathbb{R}^3$. In extension to the specific light spin $s_z \equiv \omega S_z / W$ defined in Eq. (6.5), let us define the generalized specific spin $s_{AB}$.

$$s_{AB} \equiv \frac{\left\|\vec{S}_{AB}\right\|}{W_{AB}} \equiv \frac{\left\|\mathrm{Im}\left(\vec{A}^* \times \vec{A} + \vec{B}^* \times \vec{B}\right)\right\|}{\left\|\vec{A}^* \cdot \vec{A} + \vec{B}^* \cdot \vec{B}\right\|}. \tag{9.2}$$

Our concern is then how to prove the boundedness of $s_{AB}$. To this end, let us consider the sign of $1-(s_{AB})^2$. By way of Cartesian components,

$$\begin{aligned}
&\left|\vec{A}^* \cdot \vec{A} + \vec{B}^* \cdot \vec{B}\right|^2 \left[1-(s_{AB})^2\right] \\
&= \left(A_x^* A_x + A_y^* A_y + A_z^* A_z + B_x^* B_x + B_y^* B_y + B_z^* B_z\right)^2 \\
&\quad -4\left[\mathrm{Im}\left(A_y^* A_z\right) + \mathrm{Im}\left(B_y^* B_z\right)\right]^2 \\
&\quad -4\left[\mathrm{Im}\left(A_z^* A_x\right) + \mathrm{Im}\left(B_z^* B_x\right)\right]^2 \\
&\quad -4\left[\mathrm{Im}\left(A_x^* A_y\right) + \mathrm{Im}\left(B_x^* B_y\right)\right]^2
\end{aligned} \tag{9.3}$$

Unlike the inequality in Eq. (6.7), we find it is impossible to prove that $|s_{AB}| \le 1$, without additional information such as that obtainable, for instance, form Maxwell's equations. The reason is that cross-products such as $\mathrm{Im}\left(A_y^* A_z\right)\mathrm{Im}\left(B_y^* B_z\right)$ are harder to handle in the fourth-order polynomials in Eq. (9.3).

The dispersion relation for the combined TE and TM waves is well-known, for instance, as in [9]. Its numerical solutions are easily obtainable as well. Our own computational results show that $|s_{AB}| \le 1$. But, its analytic proof as attempted by Eq. (9.3) cannot be made, thus being left as an open problem.

## 10. Conclusion

In summary, we have revisited the plasmonic resonances around a metallic nanowire, but in the presence of both energy absorption and energy radiation. According to several analytical formulas derived in this study and attendant computational data, the Poynting vectors, transverse light spins, and electric-field polarizations are found to show interesting new features according as the energy exchanges are taken into consideration. In particular, an upper bound was analytically found for specific spins. The neutral states implying energy balances were examined for their stability. All the analytical tools we have developed in this study would serve as stepping stones on which we could build more exquisite and delicate formulas as problem complexities increase and hence solutions to Maxwell's equations are harder to be obtained.

## Additional file

**Additional file 1:** This Additional file is generated by increasing the starting $m_0$, but with a slightly different scaling. After its inception with $m_0 = 0$ below the axis at $\bar{A}_i = 0$, a comet-like connecting curve appears to make three turns with increasing $m_0$ before approaching the origin. There are two of such turns across the $\bar{A}_i = 0$-line, and a single turn below the line $\bar{A}_i = 0$-line. How each frame is generated is explained as the caption for Fig. 11. (MP4 4826 kb)

**Acknowledgements**
This study has been supported by the National Research Foundation (NRF) of Republic of Korea (Grant Numbers: NRF-2011-0023612 and NRF-2015R1D1A1A01056698). We are grateful to Prof. Kwon Park of KIAS in Seoul for telling us the story of flat lands as regards topological physics.

**Author details**
[1]Research Institute of Mathematics, Seoul National University, Gwanak-gu, Seoul 08826, South Korea. [2]Department of Industrial and Management Engineering, Sunmoon University, Asan, Choongnam 31460, South Korea. [3]Computational Sciences, Korea Institute for Advanced Study, Dongdaemun-gu, Seoul 02455, South Korea.

Received: 1 November 2015 Revised: 10 February 2016
Accepted: 11 March 2016 Published online: 04 April 2016

**References**

1. Abbott, EA: Flatland. Seely & Co., United Kingdom (1884)
2. Abramowitz, M, Stegun, NC: Handbook of Mathematical Functions. Dover, New York (1970)
3. Berini, P, De Leon, I: Surface plasmon-polariton amplifiers and lasers. Nature Photon. **6**, 16–24 (2012)

4. Berry, MV: Attenuation and focusing of electromagnetic surface waves rounding gentle bends. J. Phys. A: Math. Gen. **8**, 1952 (1975)
5. Berry, MV: Phase vortex spirals. J. Phys. A: Math. Gen. **38**, L745 (2015)
6. Bliokh, KY, Nori, F: Transverse spin of a surface polariton. Phys. Rev. A **85**, 061801(R) (2012)
7. Bliokh, KY, Nori, F: Transverse and longitudinal angular momenta of light. Physics Reports **592**, 1–38 (2015)
8. Brambilla, G, Xu, F, Horak, P, Jung, Y, Koizumi, F, Sessions, NP, Koukharenko, E, Feng, X, Murugan, GS, Wilkinson, JS, Richardson, DJ: Optical fiber nanowires and microwires: fabrication and applications. Adv. Opt. Photon. **1**, 107–161 (2009)
9. Chang, DE, Sorensen, AS, Hemmer, PR, Lukin, MD: Strong coupling of single emitters to surface plasmons. Phys. Rev. B **76**, 035420 (2007)
10. Chen, Y-H, Guo, LJ: High Q long-range surface plasmon polariton modes in sub-wavelength metallic microdisk cavity. Plasmonics **6**, 183–188 (2011)
11. Costabel, M, Darrigrand, E, Sakly, H: Volume integral equations for electromagnetic scattering in two dimensions. Comput. Math. Appl. **70**(8), 2087–2101 (2015)
12. Etchegoin, PG, Le Ru, EC, Meyer, M: An analytic model for the optical properties of gold. J. Chem. Phys. **125**, 164705 (2006)
13. Foreman, MR, Swaim, JD, Vollmer, F: Whispering gallery mode sensors. Adv. Opt. Photon. **7**, 168–240 (2015)
14. Hasegawa, K, Nöckel, JU, Deutsch, M: Curvature-induced radiation of surface plasmon polaritons propagating around bends. Phys. Rev. A **75**, 063816 (2007)
15. Jackson, JD: Classical Electrodynamics, 2nd edn. Wiley, Singapore (1990)
16. Kriegsmann, GA, Taflove, A, Umashankar, KR: A new formulation of electromagnetic wave scattering using an on-surface radiation boundary condition approach. IEEE T. Antenn. Propag. **35**, 153–161 (1987)
17. Kuzmin, DA, Bychkov, IV, Shavrov, VG, Temnov, VV, Lee, H-I, Mok, J: Plasmonically induced magnetic field in graphene-coated nanowires. Opt. Lett. **41**, 396–399 (2016)
18. Kuzmin, DA, Bychkov, IV, Shavrov, VG: Influence of graphene coating on speckle-pattern rotation of light in gyrotropic optical fiber. Opt. Lett. **40**, 890–893 (2015)
19. Landau, LD, Lifshitz, EM: Fluid Mechanics, 2nd edn. Pergamon Press, (1987)
20. Lee, H-I: Wave classification and resonant excitations in lossy metal-dielectric multilayers. Photo. Nano. Fund. Appl. **8**, 183–197 (2010)
21. Lee, H-I, Mok, J: Gain-assisted poynting-vector vortices realized with a single lossy metal wire. IEEE J. Sel. Top. Quantum Electron. **19**, 4600408 (2013)
22. Lee, H-I, Mok, J: Spin annihilations of and spin sifters for transverse electric and transverse magnetic waves in co- and counter-rotations. Beilstein J. Nanotechnol. **5**, 1887–1898 (2014)
23. Lee, H.I., Stewart, D.S.: Calculation of linear detonation instability: one-dimensional instability of plane detonation. J. Fluid Mech. **216**, 103–132 (1990)
24. Li, C-F: Spin and orbital angular momentum of a class of nonparaxial light beams having a globally defined polarization. Phys. Rev. A **80**, 063814 (2009)
25. Liaw, J-W, Chen, Y-S, Kuo, M-K: Spinning gold nanoparticles driven by circularly polarized light. J Quant Spectrosc Radiat Transfer **175**, 46–53 (2016)
26. Liaw, J-W, Wu, P-T: Dispersion relation of surface plasmon wave propagating along a curved metal-dielectric interface. Opt. Express **16**, 4945–4951 (2008)
27. Louyer, Y, Meschede, D, Rauschenbeutel, A.: Tunable whispering-gallery-mode resonators for cavity quantum electrodynamics. Phys. Rev. A **72**, 031801(R) (2005)
28. Mahariq, I, Kurt, H: On- and off-optical-resonance dynamics of dielectric microcylinders under plane wave illumination. J. Opt. Soc. Am. B **32**, 1022–1030 (2015)
29. Maier, SA: Plasmonics: Fundamentals and Applications. Springer Verlag, (2007)
30. Mondal, R, Berritta, M, Paillard, C, Singh, S, Dkhil, B, Oppeneer, PM, Bellaiche, L.: Relativistic interaction Hamiltonian coupling the angular momentum of light and the electron spin. Phys. Rev. B **92**, 100402(R) (2015)
31. Olver, PJ: Introduction to Partial Differential Equations. Undergraduate Texts in Mathematics. Springer, (2014)
32. Raghu, S, Haldane, FDM: Analogs of quantum Hall effect edge states in photonic crystals. Phys. Rev. A **78**, 033834 (2008)
33. Schot, SH: Eighty years of Sommerfeld's radiation condition. Hist. Math. **19**, 385–401 (1992)
34. Tabuchi, Y, Ishino, S, Ishikawa, T, Yamazaki, R, Usami, K, Nakamura, Y.: Hybridizing ferromagnetic magnons and microwave photons in the quantum limit. Phys. Rev. Lett. **113**, 083603 (2014)
35. Tang, Y, Cohen, AE: Enhanced enantioselectivity in excitation of chiral molecules by superchiral light. Science **332**, 333–336 (2011)
36. Torres, JP, Torner, L: Twisted Photons: Applications of Light with Orbital Angular Momentum. Wiley, (2011)
37. van de Hulst, HC: Light Scattering by Small Particles. Dover Publications, New York (1981)
38. Wu, T-L, Ou, H-J: A vector power coupling model for analyzing polarization-dependent loss of equilateral triangular $3 \times 3$ weakly fused fiber couplers. Opt. Commun. **224**, 81–88 (2003)
39. Wuestner, S, Pusch, A, Tsakmakidis, KL, Hamm, JM, Hess, O: Gain and plasmon dynamics in active negative-index metamaterials. Phil. Trans. R. Soc. A **369**, 3525–3550 (2011)
40. Zachmanoglu, EC, Thoe, DW: Introduction to Partial Differential Equations with Applications. Dover Publications, (1986)
41. Zhang, J, Li, J, Tang, S, Fang, Y, Wang, J, Huang, G, Liu, R, Zheng, L, Cui, X, Mei, Y: Whispering-gallery nanocavity plasmon-enhanced Raman spectroscopy. Sci. Rep. **5**, 15012 (2015)